Steady-state monitoring of oxygen in a high-throughput organ-on-chip platform enables rapid and non-invasive assessment of drug-induced nephrotoxicity

SCHOLARONE™
Manuscripts

Steady-state monitoring of oxygen in a high-throughput organ-on-chip platform enables rapid and non-invasive assessment of drug-induced nephrotoxicity

Samuel H. Kann[a,b], Erin M. Shaughnessey[a,c], Xin Zhang[b], Joseph L. Charest[d,e], Else M. Vedula[d]

[a] Draper Scholar, 555 Technology Square, Cambridge, MA 02139, USA
[b] Department of Mechanical Engineering, Boston University, 110 Cummington Mall, Boston, MA 02215, USA
Email: xinz@bu.edu
[c] Department of Biomedical Engineering, Tufts University, 4 Colby Street, Medford, MA 02155, USA
[d] Draper, 555 Technology Square, Cambridge, MA 02139, USA
Email: evedula@draper.com
[e] Currently at Biogen, 225 Binney Street, Cambridge, MA 02142, USA

Abstract

High-throughput, rapid and non-invasive readouts of tissue health in microfluidic kidney co-culture models would expand their capabilities for pre-clinical assessment of drug-induced nephrotoxicity. Here, we demonstrate a technique for monitoring steady state oxygen levels in PREDICT96-O$_2$, a high-throughput organ-on-chip platform with integrated optical-based oxygen sensors, for evaluation of drug-induced nephrotoxicity in a human microfluidic co-culture model of the kidney proximal tubule (PT). Oxygen consumption measurements in PREDICT96-O$_2$ detected dose and time-dependent injury responses of human PT cells to cisplatin, a drug with known toxic effects in the PT. The injury concentration threshold of cisplatin decreased exponentially from 19.8 µM after 1 day to 2.3 µM following a clinically relevant exposure duration of 5 days. Additionally, oxygen consumption measurements resulted in a more robust and expected dose-dependent injury response over multiple days of cisplatin exposure compared to colorimetric-based cytotoxicity readouts. The results of this study demonstrate the utility of steady state oxygen measurements as a rapid, non-invasive, and kinetic readout of drug-induced injury in high-throughput microfluidic kidney co-culture models.

Introduction

Pre-clinical assessment of drug-induced nephrotoxicity, injury to the kidney due to drug exposure, remains a challenge due to the failure of animal models and simple 2D cell culture to recapitulate the function of the human kidney[1]. Standard pre-clinical models for drug-induced nephrotoxicity include animals, which are expensive, raise ethical concerns, and often fail to consistently predict human relevant responses to drug treatments. Standard *in vitro* cell-based assays that culture cells in static well plates are not predictive due to the lack of physiologically relevant cues, such as flow, present in the human kidney. Additionally, standard *in vitro* toxicological readouts rely on fluorescent imaging or colorimetric-based assays that are often limited to endpoint measurements and are invasive due to the addition of labels and/or extraction of samples for analysis in a separate instrument, such as a microplate reader[2]. Furthermore, because drug-induced nephrotoxicity is thought to be dependent on exposure time in the kidney[3,4], there is a need for data collection techniques that enable non-invasive monitoring of renal tissue health in *in vitro* systems throughout the time-course of drug exposure. It is also important that new data collection techniques fit existing life science infrastructure to enable broad adoption in the drug development industry. Microfluidic organ-on-chip technology enables improved toxicological assessments due to both the capability to support human cell culture in a semi-complex microenvironment and accommodate sensors for rapid, label-free, and on-chip readouts of dynamic tissue responses during drug exposures[2]. Additionally, recently developed high-throughput organ-on-chip platforms with industry standard formats and compatibility with existing life science workflows has increased the potential for translation of organ-on-chip technology in the pharmaceutical industry[5,6].

Microfluidic organ-on-chip technology is advantageous for nephrotoxicity assessment due to its ability to support evaluation of the epithelial-microvascular endothelial structure of the proximal tubule (PT)[7–9], a primary site for transport and accumulation of nephrotoxic agents in the kidney[10], in a precisely designed microenvironment. Studies have shown that PT cells exposed to flow have improved structure[11–13], function[7,14–16], and responses to nephrotoxic

47   drug exposures[9,17] compared to cells cultured in static conditions. Also, both shear stress and increased oxygen supply
48   via flow have shown to increase oxygen consumption rates and oxygen-dependent metabolism[14,18], a key function in
49   the human PT due to its high metabolic workload[19]. The co-culture of human primary proximal tubule epithelial cells
50   (hRPTECs) and human primary microvascular endothelial cells (hMVECs) results in cross-talk between the two cell
51   types that alters PT epithelial cell metabolic activity and regulation of drug transport genes[20,21]. Also, our group
52   recently found that transepithelial electrical resistance, a functional readout of PT tissue, detected cisplatin-induced
53   toxicity with greater sensitivity for hRPTECs in co-culture compared to in monoculture[22]. Thus, inclusion of flow and
54   multiple cell types in PT-on-chips is important to recapitulate physiologically relevant PT injury responses during
55   nephrotoxic drug exposures. Additionally, high-throughput systems that support an array of independent organ-on-
56   chips are needed to assess multiple variables, such as drug concentrations, in parallel with a minimum of 3 replicates
57   for performing statistical analyses. Recently, we have published on a high-throughput platform that has been
58   developed for culturing up to 96 epithelial-endothelial barrier models on a single microtiter plate format[5,22–24].

59   Sensor integration in high-throughput organ-on-chip systems enables non-invasive and near real-time monitoring of
60   tissue health during drug exposures[2]. For example, electrical-based transepithelial-endothelial electrical resistance
61   allows rapid and non-invasive measurement of tissue barrier function for toxicological assessment[22,25]. Oxygen
62   sensing is particularly advantageous for toxicological screening because it enables measurement of oxygen
63   consumption as a readout of tissue metabolic function and viability[26]. Optical-based and electrochemical-based
64   sensors have been utilized in cell culture systems for monitoring oxygen consumption. Electrochemical-based sensing
65   systems[27–29] are generally low throughput due to the large footprint of electrical hardware and complex fabrication
66   processes[30]. Optical-based oxygen sensing is advantageous for integration in high-throughput microfluidic systems
67   due to its low footprint, straightforward integration, and fast sensor response times[31,32]. The Agilent Seahorse
68   XFeAnalyzer, a commercial optical-based oxygen sensing system, measures cell oxygen consumption rates in static
69   96 well plates, however, does not support perfusion or operate in organ-on-chip systems[33,34].   Oxygen sensor-
70   integrated organ-on-chip systems reported to date remain low-throughput with at most 24 devices contained in an
71   array[35] and with the majority containing 9 or fewer devices[29,36–40]. Previously, we reported a technique to measure
72   oxygen consumption rates in an array of organ-on-chip devices[41], but it required cycling flow on and off for 1-2
73   minutes in each device sequentially, resulting in un-stable flow conditions and a long time-duration of 1.6-3.2 hrs. for
74   measurement in all 96 devices contained in a standard microtiter plate format. Oxygen consumption readouts based
75   on steady state oxygen levels may address the above limitations by enabling continuous perfusion and a reduction in
76   the time required to sequentially collect data across a large array of devices using a single fiber optic. A recent study
77   demonstrated oxygen consumption measurements in an array of devices containing hepatocytes during continuous
78   perfusion[35], however, the culture chambers were limited to single microchannels, which do not accommodate co-
79   culture models of human tissue barriers, such as the epithelial-endothelial barrier in the PT. Therefore, there is a need
80   for investigation of new high-throughput oxygen sensing techniques that enable non-invasive monitoring of metabolic
81   activity and viability during continuous flow in systems that support tissue barrier models, whether comprised of
82   single or multiple cell types.

83   In this study, we investigated a technique for the measurement of steady state oxygen levels in PREDICT96-O_2 (P96-
84   O_2), a high-throughput microfluidic organ-on-chip platform with integrated optical-based oxygen sensors, for
85   monitoring oxygen consumption and assessment of drug-induced injury in a microfluidic human primary co-culture
86   model of the kidney PT (mcPT). Oxygen consumption measurements enabled detection of a dose and time-dependent
87   injury response to cisplatin, a nephrotoxic compound, during a clinically relevant 5-day exposure duration.
88   Measurement of a dose and time-dependent injury response to cisplatin allowed rapid prediction of an injury
89   concentration threshold as a function of exposure time in the mcPT. Finally, we compared the performance of oxygen
90   consumption and gold standard colorimetric-based cytotoxicity readouts for monitoring drug-induced injury in the
91   mcPT. Our results demonstrated a new utility of oxygen sensing and associated methodology in a high-throughput
92   organ-on-chip platform for pre-clinical evaluation of drug-induced nephrotoxicity and investigation of renoprotective
93   strategies.

Results and discussion

Design and workflow for oxygen-sensing in P96-O_2 and assessment of drug-induced PT injury

96   We developed a workflow to assess oxygen consumption and drug-induced injury to hRPTECs in a mcPT during
97   continuous perfusion. P96-O_2 contained an array of 96 organ-on-chip devices with integrated optical-based oxygen
98   sensors in a microtiter plate format similar to an industry standard well plate commonly used in drug development[5,41].
99   Fig. 1a. shows an image of the bottom of a P96-O_2 culture plate. Each device of the P96-O_2, shown schematically in
100 fig. 1b., was constructed in a membrane bilayer format, which consisted of top and bottom microchannels separated
101 by a porous membrane. The plate was constructed primarily from cyclo-olefin polymer, a thermoplastic with low
102 oxygen permeability. Each device contained a single oxygen sensor bonded to the floor of the bottom microchannel
103 in the center of the overlap region between the top and bottom microchannels, as shown in fig. 1b-c. The mcPT
104 consisted of hRPTECs and human primary microvascular endothelial cells (hMVECs) on the bottom and top of the
105 membrane, respectively, as shown schematically in fig. 1c. For mimicking the flow conditions in the PT[42],
106 unidirectional and recirculating perfusion in the top and bottom microchannels provided convection-based delivery of
107 a nephrotoxic compound (illustrated as purple dots in fig. 1c.) to hRPTECs cultured on the membrane. hMVECs
108 cultured on the top side of the membrane, shown in fig. 1d. and hRPTECs on the bottom of the membrane, shown in
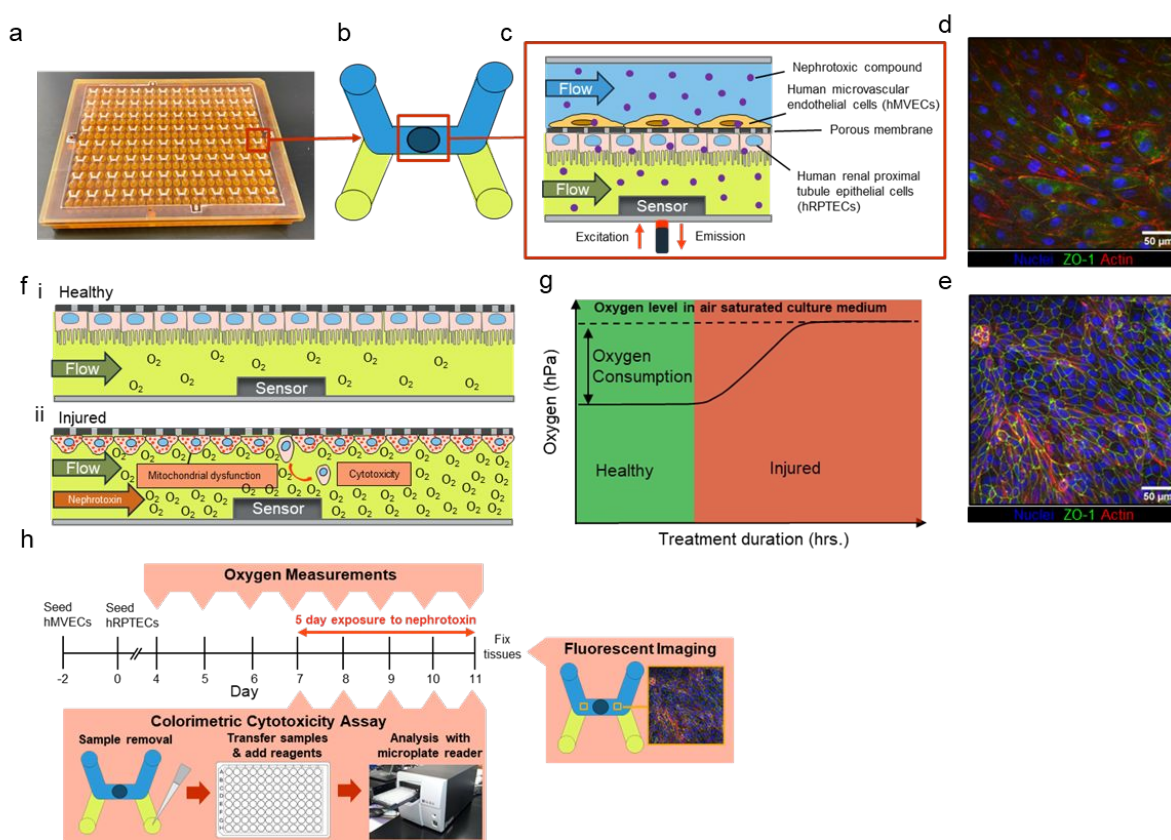
Figure 1: **Experimental design and workflow for oxygen sensing and assessment of drug-induced nephrotoxicity in a human microfluidic co-culture PT model.** a) Bottom view of a P96-O_2 plate with 96 organ-on-chip devices. b) Schematic of a single device with a top (blue) and bottom microchannel (green) and an oxygen sensor located centrally on the floor of the bottom microchannel. c) A schematic that highlights the key components for assessment of drug-induced nephrotoxicity in P96-O_2. hMVECs and hRPTECs cultured on the top and bottom surfaces of the porous membrane, respectively, were exposed to a nephrotoxic compound (purple dots) via controlled and unidirectional flow in the top and bottom microchannels. An optical-based oxygen sensor located in the bottom microchannel measured oxygen via a fiber optic and commercial oxygen meter. Confocal images of d) hMVECs and e) hRPTECs stained for nuclei (blue), actin (red), and ZO-1 (green) formed confluent monolayers on the membrane. f) Schematic illustrating an increase in steady state oxygen levels that occurs in the bottom microchannel following injury to the hRPTECs. g) Illustration depicting an increase in steady state oxygen levels over time as hRPTECs undergo injury during exposure to a nephrotoxic compound. h) Experimental timeline for co-culture and assessment of drug-induced nephrotoxicity in P96-O_2.

109   fig. 1e. after 11 days of co-culture in P96-O$_2$ demonstrated monolayer formation of both cell types. hRPTECs had high
110   barrier integrity, visualized via expression of tight junction protein ZO-1, and displayed a cobblestone-like
111   morphology, as shown in fig. 1e. An optical-based sensor in each device measured steady state oxygen levels during
112   continuous perfusion and delivery of a nephrotoxic compound in the bottom microchannel. The schematics in fig. 1f.
113   illustrate the working principle of our sensing technique which relies on a change in steady state oxygen levels that
114   occurs in the bottom microchannel as hRPTECs transition from healthy (fig. 1fi) to injured (fig. 1fii) during a
115   nephrotoxic drug exposure. Fig. 1g. illustrates an expected qualitative increase in oxygen levels as the hRPTECs
116   undergo injury and consume less oxygen over time following a nephrotoxic exposure. P96-O$_2$ and our experimental
117   workflow, shown in fig. 1h., allowed assessment of drug-induced injury during a 5-day exposure to cisplatin, a
118   nephrotoxic drug, via oxygen sensing, a conventional colorimetric cytotoxicity assay, and endpoint fluorescent
119   imaging. The P96-O$_2$ platform was well-suited for studying drug-induced nephrotoxicity in the human PT barrier due
120   to its high-throughput capability to co-culture PT epithelial and microvascular endothelial cells in a fluidic
121   environment and simultaneously monitor oxygen in the microchannel containing hRPTECs. P96-O$_2$ provided an
122   improvement in throughput over existing systems that contain at most 24 devices[29,35,36,43]. Additionally, the membrane
123   bilayer format of each device in P96-O$_2$ provided benefit over single microchannels utilized in existing high-
124   throughput systems[35] for modelling multi-cell type tissue barriers with perfusion on both sides, such as the PT barrier.

Detection of oxygen consumption in the mcPT during continuous perfusion

126   We developed an approach to monitor steady state oxygen levels in the bottom microchannel of all 96 devices in P96-
127   O$_2$ for rapid, label-free, and on-chip detection of oxygen consumption of hRPTECs. A fiber optic positioned beneath
128   each sensor spot sequentially, shown in fig. 2a., measured oxygen via a commercial oxygen meter (Pyroscience,
129   Germany) during continuous perfusion and recirculation of media in the top and bottom microchannels. Oxygen was
130   measured, shown schematically in fig. 2b., via automated and sequential positioning of the fiber optic beneath each
131   sensor using a standard programmable microscope stage. 10-12 data samples were acquired in each device, shown in
132   fig. S1a., resulting in a total duration of 32 minutes for automated measurement of oxygen in all 96 devices in P96-
133   O$_2$. The 10-12 oxygen samples acquired in each device had negligible variability with an average standard deviation
134   of 0.25 ± 0.1 hPa (n=96 devices), shown in fig. S1b., which indicated that oxygen measurements were steady with
135   respect to time during each device measurement period. During oxygen measurements, P96-O$_2$ devices contained
136   hRPTECs + hMVECs, hRPTECs only, or no tissue conditions, as shown in the plate format in fig. S2. A representative
137   example of the average steady state oxygen levels measured in each device of a single P96-O$_2$ plate containing devices
138   with tissue and without tissue was shown in fig. 2c. Oxygen levels in devices containing tissue were slightly lower
139   near the center of the plate, compared to devices located at the edge, shown in fig. S3b, which was likely due to greater
140   oxygen supply at the periphery of the plate. Despite variability in oxygen levels, the relative change in oxygen over
141   24 hours in each device did not depend significantly (p=0.28) on each device's position within the plate, as shown in
142   fig. S3d. Further work is still needed to investigate potential variability due to device position within a plate for
143   durations longer than 24 hours, in which proliferation or changes in cellular respiration can occur. Oxygen was
144   significantly lower ($p < 0.001$) in devices containing hRPTECs + hMVECs and hRPTECs only compared to control
145   devices containing water and culture medium only, shown in fig. 2d. There was no significant difference ($p > 0.05$)
146   between oxygen levels in devices containing hRPTECs and hMVECs compared to those with hRPTECs only, which
147   indicated that oxygen measurements in the bottom microchannel were sensitive to hRPTEC oxygen consumption with
148   negligible contribution from hMVECs in the top microchannel. Fig. 2e. shows oxygen measurements in devices
149   containing hRPTECs and hMVECs compared to control devices containing water and culture medium over the course
150   of 8 days. Oxygen levels in control devices containing water and culture medium remained steady near 200 hPa, the
151   partial pressure of oxygen in water equilibrated in air. Oxygen levels in devices containing hRPTECs and hMVECs
152   was significantly lower than oxygen in the water and culture medium controls, as shown in fig. 2e. Oxygen
153   consumption was estimated as the difference between steady state oxygen levels in devices containing tissue and
154   devices containing only culture medium. Oxygen consumption increased over time during 7 days of culture in P96-
155   O$_2$, as shown in fig. 2f. Oxygen consumption was significantly greater in devices containing hRPTECs and hMVECs
156   compared to devices containing only culture medium over 8 days of culture. The increase in oxygen consumption over
157   8 days, shown in fig. 2f., is likely attributed to continued proliferation of hRPTECs, which was supported by hRPTEC
158   expression of Ki67, a protein associated with proliferation, following 10 days of culture in the mcPT, shown in Fig.
159   S4.
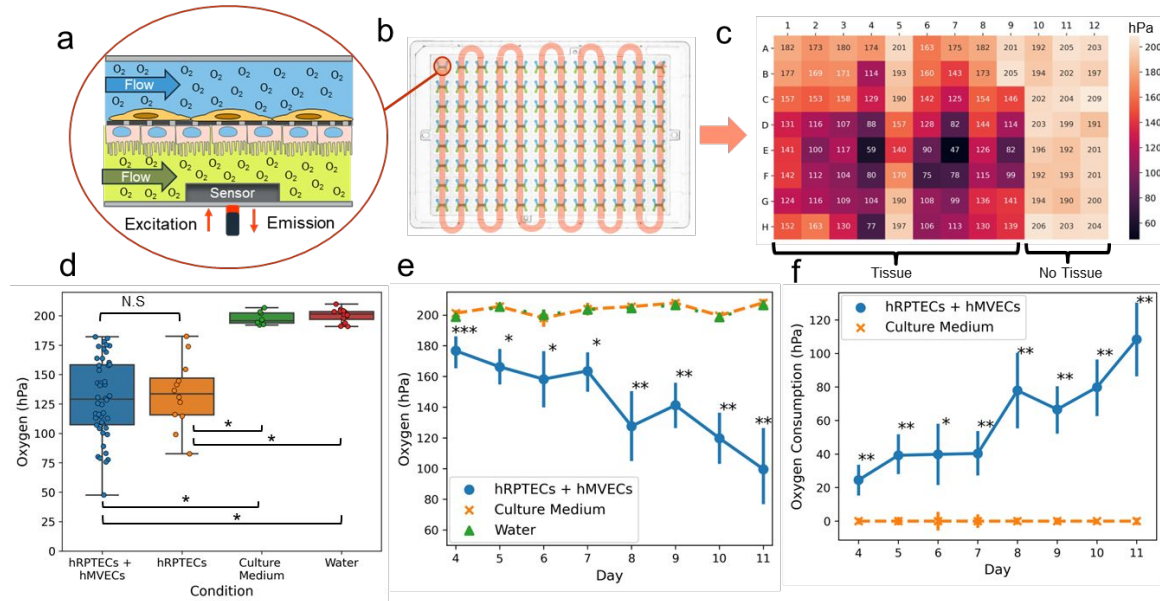
Figure 2: Steady state oxygen measurements in the bottom microchannel enabled detection of hRPTEC consumption in each mcPT. a) Schematic of a single device with online oxygen measurements in the bottom microchannel. b) Illustration of the path of the fiber optic during sequential oxygen measurements in an entire P96-O₂ plate. c) Representative heatmap displaying steady state oxygen readouts across an entire P96-O₂ plate with devices containing tissue and no tissue controls d) Oxygen measurements in tissue devices containing hRPTECs + hMVECs (n=46) and only hRPTECs (n=12) compared to control devices containing culture medium (n=8) and water (n=8) on day 6 of culture (N.S. p = 0.8, *p < 0.001, Kruskal-Wallis and Dunn's post-hoc test). e) Oxygen and f) oxygen consumption measurements on days 4-11 in devices containing hRPTECs +hMVECs (n=5) compared to devices containing water (n=16) and culture medium (n=4) (*p < 0.05, **p < 0.01, ***p < 0.001 compared to culture medium controls, Kruskal-Wallis and Dunn's post-hoc test).

160   The presented technique for monitoring oxygen consumption provided novelty and improvement over existing
161   methods due to the combination of 1) high-throughput acquisition (96 devices/32 minutes), 2) compatibility with
162   tissue models consisting of multiple cell types in a membrane bi-layer format, 3) capability to detect oxygen
163   consumption during continuous perfusion and 4) minimal hardware requirements and simple setup for measurements.
164   The commercial Agilent Seahorse XFeAnalyzer can measure oxygen consumption in 96 wells in 2 minutes[44],
165   however, does not operate in organ-on-chip systems. Existing techniques for measurement of oxygen consumption in
166   high-throughput organ-on-chip systems have several limitations including the necessity to modulate flow on and off[41],
167   the large footprint and complex integration of sensing hardware[35], and limitation of measurements to a single
168   monolayer of cells[35,36]. While steady state oxygen levels provided an indicator of oxygen consumption in the hRPTEC
169   channel, further work is needed to investigate the relationship between steady state oxygen levels and hRPTEC oxygen
170   consumption rates in P96-O₂. In future work, finite element analysis-based models could be employed to estimate
171   hRPTEC oxygen consumption rates from steady state oxygen measurements, similar to an approach reported in Moya
172   et al[29]. Additionally, this technique for monitoring oxygen consumption is immediately applicable to a broad range of
173   studies that utilize a microfluidic membrane bi-layer format for culturing complex tissue models including the gut
174   intestines[45], lung[24], blood brain barrier[46], and liver[47]. Finally, only a single fiber optic was required to achieve
175   measurements in 96 devices, which resulted in a significantly lower footprint and simpler fabrication and set up
176   compared to current systems[35].

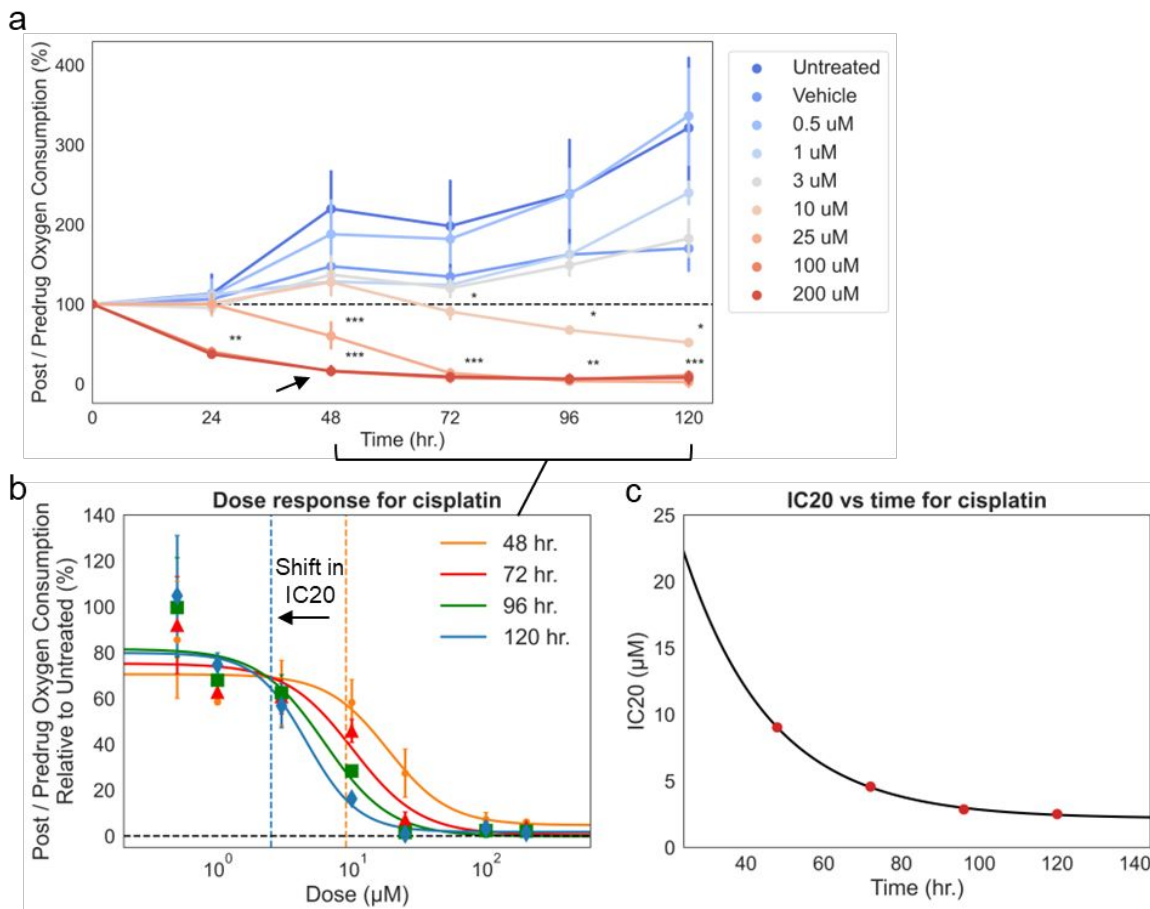**Oxygen sensor-enabled monitoring of cisplatin-induced nephrotoxicity**

178   Measurement of oxygen consumption in P96-O₂ during continuous perfusion enabled non-invasive monitoring of
179   drug-induced nephrotoxicity during a clinically relevant 5-day exposure duration to cisplatin[48], a compound with
180   nephrotoxic effects in the human PT[49]. Representative images of hRPTECs stained with nuclei, actin, and ZO-1,
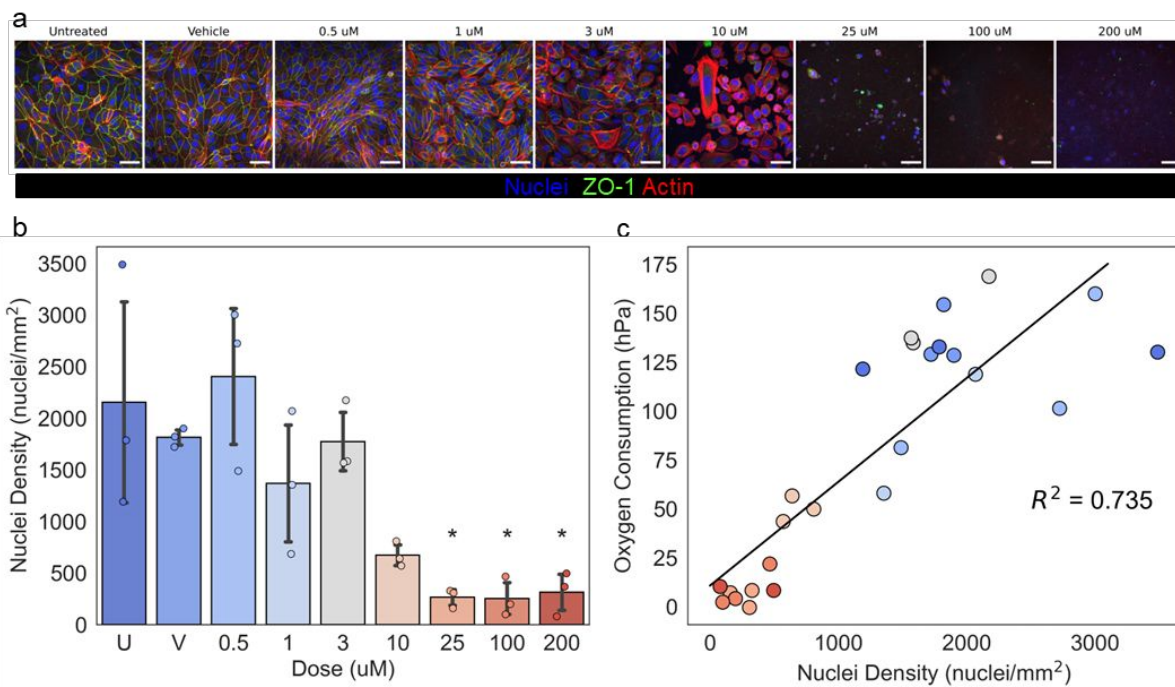
Figure 3: Oxygen consumption correlated with hRPTEC nuclei density in the mcPT following 5 days of cisplatin exposure. a) Representative confocal images of hRPTECs on the membrane stained with nuclei, actin, and ZO-1 (scalebar = 50 μm) and b) density of hRPTEC nuclei on the membrane for each dose of cisplatin following 5 days of treatment (* $p < 0.05$ relative to untreated group, Kruskal-Wallis and Dunn's post hoc test). c) Correlation between oxygen consumption measurements and density of hRPTEC nuclei on the membrane ($R^2 = 0.735$, $p < 0.001$, n=25).

181   shown in fig. 3a., indicated a dose-dependent injury response following 5 days of exposure to cisplatin. Dose-
182   dependent cytotoxicity was evident due to changes in the hRPTEC nuclei density on day 5, as shown in fig. 3b.
183   Additionally, there was a dose-dependent reduction in the expression of key structural proteins actin and ZO-1, shown
184   in fig. 3a. and fig. S5. hRPTEC nuclei density was significantly lower than the untreated group at 25, 100, and 200
185   μM ($p < 0.05$). Oxygen consumption on day 5 of the cisplatin exposure correlated with hRPTEC nuclei density with
186   an R^2 value of 0.735 ($p < 0.001$), as shown in fig. 3c. This correlation indicated oxygen consumption could be utilized
187   as a label-free, non-invasive, and rapid surrogate indicator of hRPTEC density decrease and injury in P96-O_2.

188   Post/predrug oxygen consumption in the mcPT was defined as oxygen consumption over the course of
189   cisplatin exposure relative to oxygen consumption measured prior to the initial exposure at t = 0 hrs. Doses of cisplatin
190   were delivered in P96-O_2 according to the plate format shown in fig. S6. We did not expect significant biases in the
191   post/predrug oxygen consumption readouts due to the plate format design. This was because the post/predrug oxygen
192   consumption readouts were based on relative changes in oxygen over time in each device, which did not depend
193   significantly on each device's position within the plate, as shown in fig. S3d. Post/predrug oxygen consumption,
194   shown in fig. 4a., was measured at 24 hr. timepoints for 5 days during exposure of hRPTECs to cisplatin and a time-
195   and dose-dependent response was observed. Within 24 hrs., post/predrug oxygen consumption in devices treated with
196   100 and 200 μM decreased significantly relative to the untreated devices ($p < 0.01$). At 48 hrs., post/predrug oxygen
197   consumption in devices treated with 25 μM decreased significantly relative to the untreated devices ($p < 0.001$). At
198   72 hrs., post/predrug oxygen consumption in devices treated with 10 μM decreased significantly relative to the
199   untreated devices ($p < 0.05$). There was no significant decrease in post/predrug oxygen consumption in devices treated
200   in the range of 0-3 μM. Post/predrug oxygen consumption in devices treated with 0-3 μM increased above 100% over
201   time, which was most likely due to proliferation of hRPTECs in the bottom microchannel, as discussed previously.

Figure 4: Oxygen sensor-enabled monitoring of cisplatin-induced injury to hRPTECs in the mcPT. A) Post/predrug oxygen consumption measurements over time for a range of cisplatin doses. Maximal injury response occurred within 48 hrs (black arrow). b) Dose-dependent reduction in post/predrug oxygen consumption (markers) with fitted hill equations (solid lines) for estimation of the IC20 at different timepoints. The IC20s at 48 and 120 hrs. are shown as orange and blue dotted lines, respectively. g) The IC20 (red circles) for cisplatin decreased exponentially over time in the mcPT. Data are mean ± standard deviation of n=4-6 devices per dose. *p < 0.05, **p < 0.01, ***p < 0.001 relative to untreated (Kruskal-Wallis and Dunn's post-hoc test).

202   Dose response curves based on the conventional 4-parameter Hill equation[50,51] were estimated for data
203   collected at 48, 72, 96, and 120 hrs. for prediction of an IC20, the concentration at which 20% reduction in post/predrug
204   oxygen consumption was observed. Maximal injury in the mcPT was observed at 48 hrs., indicated by a black arrow
205   in fig. 4a. Therefore, data collected prior to 48 hrs. was not included in the hill function curve fitting. Fig. 4b. shows
206   dose response curves (solid lines) and experimental data (markers) for each timepoint from 48-120 hrs. of cisplatin
207   exposure. The IC20 decreased as exposure to cisplatin increased between the 48 and 120 hr. timepoints, shown as
208   orange and blue dotted lines, respectively, in fig. 4b. and followed an exponential decay, shown in fig. 4c. The fitted
209   exponential, shown in equation 1, fit the experimental data closely with an R^2 of 1.00 and predicted a long-term IC20
210   of 2.2 μM. The predicted IC20s at 24 hr. timepoints over 5 days were provided in table 1 below.

211                         $$IC20(t) = 58.46\, e^{-0.045t} + 2.16 \qquad (1)$$

212   Table 1: Summary of predicted IC20s during a 5-day exposure to cisplatin

Timepoint (hr.)	24	48	72	96	120	infinity

|	IC20 (μM)	19.8	7.5	3.8	2.7	2.3	2.2

213

214 These results demonstrated a new capability of a high-throughput oxygen sensor integrated organ-on-chip platform to
215 rapidly predict a time-dependent concentration threshold at which drug-induced injury occurs in a human PT model.
216 The 5-day IC20 for cisplatin of 2.3 μM was below expected blood concentrations of cisplatin reported in 5-day
217 infusions[48], which may explain the prevalence of cisplatin-induced kidney injury in the clinic. Additionally, the time-
218 dependent decrease in the IC20 of cisplatin in the mcPT supports data in animal models suggesting that cisplatin-
219 induced kidney injury is dose and time-dependent[3,4]. Our predicted 5-day IC20 in the mcPT was in close agreement
220 with a 5-day cisplatin toxicity threshold of 2.8 μM predicted using perfused vascularized human kidney spheroids[52].
221 Interestingly, the toxicity thresholds for cisplatin were similar for hRPTECs cultured in spheroids and a membrane
222 bilayer format, despite significant differences in the tissue architecture between the two systems. While spheroids
223 have shown promise for toxicological studies[52], there are key advantages of performing toxicological assessments in
224 membrane bilayer formats including access to both apical and basal surfaces of the tissue layer for transport studies,
225 independent control of flow rates[5,22] in each microchannel, and compatibility with barrier-specific assays[53,54]. We
226 believe that this system and the oxygen measurement technique could aid clinicians and drug developers in optimizing
227 treatment regimens of nephrotoxic agents and investigation of protective strategies for mitigation of drug-induced
228 nephrotoxicity. Additionally, this technique is broadly applicable for toxicological assessment in other complex tissue
229 models that utilize a membrane bilayer format[47,55,45,24].

Oxygen vs colorimetric-based measurements for monitoring hRPTEC injury

231 We compared our oxygen sensing technique with the CyQUANT™ LDH Cytotoxicity assay, a commercial
232 colorimetric-based assay, for assessment of hRPTEC injury during the 5-day exposure to cisplatin. The CyQUANT™
233 assay quantifies cytotoxicity via extraction of cell culture medium from each device and measurement of the amount
234 of lactate dehydrogenase (LDH), an enzyme in healthy cells that is released upon damage to the cell membrane. Fig.
235 5a-b. shows cumulative LDH, the total LDH released in culture medium relative to t=0hr., and post/predrug oxygen
236 consumption for doses in the range of 0-200 μM and at 24 hr. timepoints. Both cumulative LDH and post/predrug
237 oxygen consumption readouts displayed an expected dose-dependent response at the early timepoints of 24 and 48
238 hrs. of exposure. Interestingly, between 72-120 hrs., post/predrug oxygen consumption continued to display an
239 expected dose-dependent trend, whereas cumulative LDH did not. Specifically, cumulative LDH in the middle dose
240 groups of 10 and 25 μM was higher than in the high dose groups of 100 and 200 μM, as shown in fig. 5a., which was
241 not consistent with the dose response in the post/predrug oxygen consumption readouts, data from other studies[22], and
242 the general expectation that injury increases with dose of a toxic drug. This inconsistency was likely due to differences
243 in the time at which maximum cytotoxicity, quantified via LDH release, occurred between the middle and high dose
244 groups. Specifically, maximum cytotoxicity occurred within 24 hrs. in the high dose group compared to 48-96 hrs. in
245 the middle dose group, as shown in fig. S7. We found that the combination of different timepoints of maximum
246 cytotoxicity and expected hRPTEC proliferation over time to likely be significant factors leading to an unexpected
247 dose-dependent response in the cumulative LDH readouts between 72-120 hrs. On the other hand, post/predrug oxygen
248 consumption readouts resulted in an expected dose-response at all timepoints similar to dose-response data for
249 cisplatin reported in other studies[22,52]. Therefore, we found post/predrug oxygen consumption to be a more robust and
250 consistent metric for evaluating dose-dependent injury over multiple days of exposure compared to cumulative LDH.
251 It should be noted that post/predrug oxygen consumption in the vehicle group was slightly lower than the untreated
252 and low dose groups. This was likely due to a higher concentration of saline present in the vehicle group compared to
253 the untreated and low dose groups, to maintain equivalent concentrations of saline between the vehicle and highest
254 dose groups.

255 Combination of post/predrug oxygen consumption and cumulative LDH readouts for each mcPT allowed
256 visualization of the time-dependent formation of two distinct clusters of mcPTs representing healthy and injured tissue
257 following 5 days of cisplatin exposure. Fig. 5c. shows the relationship between post/predrug oxygen consumption and
258 cumulative LDH readouts at each timepoint during cisplatin exposure, in which each datapoint represents an individual
259 mcPT. Unsupervised classification, based on probabilistic gaussian mixture models[56], of the datapoints in fig. 5c. into
260 two distinct clusters resulted in prediction of mcPTs that were healthy or injured. At 120 hrs., the predicted healthy
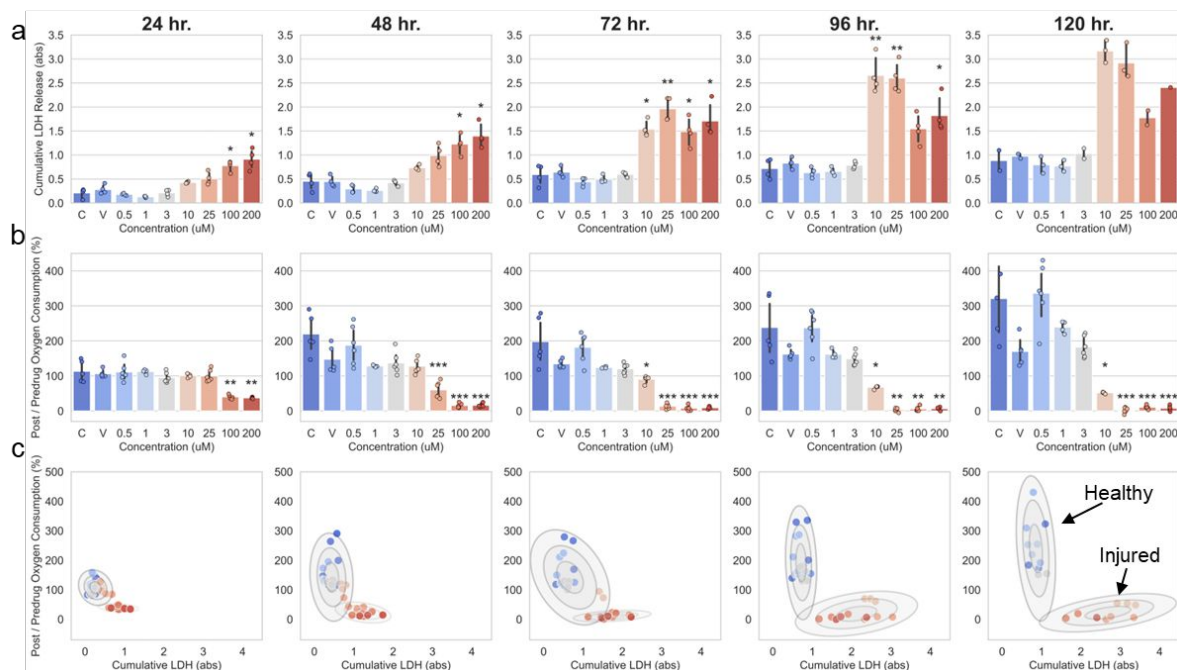
Figure 5: Comparison between oxygen consumption and colorimetric-based cytotoxicity readouts for monitoring hRPTEC injury in the mcPT. a) Cumulative LDH in the hRPTEC microchannel and b) post/predrug oxygen consumption for each timepoint during exposure of hRPTECs to cisplatin for 5 days (*$p < 0.05$, **$p < 0.01$, ***$p < 0.0001$ relative to untreated within each timepoint between 24-96 hr. using Kruskal-Wallis and Dunn's post-hoc test). There were insufficient replicates in cumulative LDH data at 120 hr. for statistical testing. c) Unsupervised clustering of individual mcPTs into separate groups, representing healthy and injured tissue, at each timepoint based on post/predrug oxygen consumption and cumulative LDH data.

261 and injured clusters contained mcPTs in the 0-3 μM and 10-200 μM range, respectively, which supported image-based
262 observations of cell death occurring in the 10-200 μM range at 120 hrs., shown previously in fig. 3a-b. Changes in the
263 shapes of the two clusters and in the occupancy of mcPTs in each cluster over time, shown in fig. 5c., were dynamic
264 indicators of injury occurring in the mcPT based on two different metrics of cell health. Specifically, between 24-96
265 hrs., mcPTs exposed to cisplatin in the range of 10-25 μM switched occupancy from the healthy cluster to the injured
266 cluster.
267   Our reported method for measurement of steady state oxygen levels has key advantages over conventional
268 colorimetric-based assays, as summarized in table 2 below. Additionally, we found that monitoring oxygen levels in
269 P96-O$_2$ allowed measurement of an expected dose-dependent injury response for cisplatin across all timepoints during
270 a 5-day drug exposure. This demonstrated a key advantage over cumulative LDH readouts, which resulted in a dose-
271 response that was inconsistent with expectations between 72-120 hrs. of exposure. Additionally, we showed that the
272 combination of oxygen consumption measurements and colorimetric-based cytotoxicity readouts in P96-O$_2$ allowed
273 visualization of distinct clusters, representing healthy and injured mcPTs, which provided a useful new readout for
274 monitoring the progression of injury in mcPTs during multiple-day drug exposures.

275   Table 2: Key advantages of oxygen sensing compared to colorimetric-based assays for toxicological assessment in high-
276   throughput microfluidic organ-on-chip systems

Key performance metrics	Oxygen sensing	Colorimetric-based assay
Data collection speed	32 min. / plate *	~1-2 hr. / plate
On-chip measurements	Yes; label-free & non-invasive	No; Requires extraction of culture medium and multiple liquid handling steps
Enables perfusion during data collection	Yes	No

Chemical reagents required	No	Yes

277 *An additional 30-45 minutes was required for a P96-O_2 plate to reach temperature equilibrium prior to oxygen measurements.

Conclusions

279 For the first time, we demonstrated a technique to monitor oxygen consumption during continuous perfusion in 96
280 mcPTs within 32 minutes, which enabled rapid and non-invasive assessment of drug-induced nephrotoxicity. Oxygen
281 consumption measurements detected time and dose-dependent injury responses to cisplatin, a nephrotoxic drug, during
282 a clinically relevant 5-day exposure duration. The IC20 of cisplatin decreased as a function of exposure time in the
283 mcPT, which agreed with findings in animal studies and in other *in vitro* models that cisplatin toxicity is dose and
284 time dependent. Furthermore, the 5-day IC20 in the mcPT was below clinically reported blood concentrations of
285 cisplatin during 5-day infusions[48], supporting incidences of cisplatin-induced kidney injury in the clinic. Also, oxygen
286 consumption readouts in the mcPT provided more robust and expected dose-response data than conventional
287 colorimetric-based cytotoxicity readouts at later timepoints of cisplatin exposure. Our results demonstrated the utility
288 of monitoring steady state oxygen levels in a high-throughput organ-on-chip platform for non-invasive and rapid
289 assessment of oxygen consumption and nephrotoxicity in a human co-culture PT model. The presented technique will
290 provide a valuable tool in drug development for evaluating injury in microfluidic kidney models for toxicological
291 screening and investigation of potential therapies.

Experimental

Cell culture

294 Primary human renal proximal tubule epithelial cells (hRPTECs) were purchased from ScienCell Research
295 Laboratories (Lot: 5340) and expanded through passage 5 prior to seeding in P96-O_2 plates. hRPTECs were cultured
296 in culture medium consisting of 50:50 DMEM/F12 (Gibco, USA) supplemented with 0.5% fetal bovine serum (Life
297 Technologies, USA), 10 ng/mL recombinant human epidermal growth factor (Thermo Fisher, USA), 5 μg/mL insulin
298 (Sigma-Aldrich, USA), 6.5 ng/mL 3,3',5-triiodo-L-thyronine sodium salt (Sigma-Aldrich, USA), 10 μg/mL human
299 transferrin (Sigma-Aldrich, USA), and 1% penicillin-streptomycin (Thermo Fisher, USA). Primary human dermal
300 microvascular endothelial cells (hMVECS) were purchased from Lonza (CC-2543) and expanded through passage 6.
301 hMVECs were cultured in a commercial medium kit (CC-3156, Lonza, USA) consisting of EBM™-2 Basal Medium
302 (CC-3156) and EGM™-2 MV microvascular endothelial cell growth medium supplements (CC-4146). hRPTECs
303 were cultured in a T-150 flask (Thermo Fisher, USA) with 30 mL of hRPTEC culture medium for 2 days prior to
304 seeding in P96-O_2. hMVECs were cultured in a T-150 flask coated with 1μg/cm^2 human plasma fibronectin with 30
305 mL of hMVEC culture medium for 2 days prior to seeding in P96-O_2.

Preparation of the P96-O_2 and micropump array

307 The fabrication of the P96-O_2 culture plates and micropump array was described previously in detail[5,41]. Briefly, P96-
308 O_2 plates contained 96 optical-based oxygen-sensitive sensor spots (0.75 mm in diameter and 50 μm thick) that were
309 cut from a sheet of photosensitive oxygen sensor foil (item No. OXFOIL-TN, Pyroscience, Germany). Each P96-O_2
310 plate contained an 11 μm thick polycarbonate track-etched porous membrane with a pore diameter of 1 μm (Sterlitech,
311 WA, USA). P96-O_2 plates and the micropump array were sterilized with ethylene oxide exposure for 24 hours,
312 followed by a minimum of 48 hours of degassing. P96-O_2 plates were treated with oxygen plasma for 60 seconds to
313 increase the hydrophilicity of the microchannel surfaces. Microchannels of the P96-O_2 were filled with 70% ethanol
314 and subsequently rinsed 3 times with phosphate-buffered saline (PBS).

Cell seeding in P96-O_2

316 Prior to seeding cells in P96-O_2, each microchannel was filled with a solution of 60 μg/mL of collagen IV from human
317 placenta (Cat #: CC076, Sigma Aldrich, USA) in PBS and the plate was placed on a rocker for 1 hour at room
318 temperature. Co-cultures of hMVECs and hRPTECs and monocultures of hRPTECs were cultured in specified regions
319 of the P96-O2 plate, as shown in the plate map in fig. S2. hMVECs were seeded in the top microchannel two days
320 prior to seeding of hRPTECs in the bottom microchannel. 30 μL of a 1 million/mL cell suspension was delivered to

321 the inlet of each top microchannel via a gravity seeding method previously described[5]. For seeding of hRPTECs, 30
322 μL of a 1 million/mL cell suspension was delivered to the inlet of each bottom microchannel and the plate was
323 subsequently flipped face-down and incubated at 37° C for 1 hour to allow cells to adhere to the porous membrane.
324 Devices with suboptimal cell densities below approximately 500 cells/mm^2 (25% of the expected density) were
325 identified as outliers following cell seeding via phase contrast imaging. Suboptimal densities likely occurred due to
326 error sources in the cell seeding process including low seeding densities and introduction of bubbles that interfere with
327 adhesion. 14 devices were identified as outliers and excluded from all data presented in this manuscript. Following 1
328 hour, the plate was flipped face-up, culture medium in each microchannel was refreshed, and flow was initiated at 1
329 μL/min (0.01 dyne/cm^2) for 1 day. Flow was increased to 70 μL/min (0.73 dyne/cm^2) on day 2 for the remainder of
330 the experiment and the culture medium in each microchannel was refreshed daily.

Oxygen consumption measurements

332 Oxygen measurements were acquired with a commercial optical oxygen meter, optical fiber, and software
333 (FireStingO$_2$, Pyroscience, Germany). P96-O$_2$ was placed in a standard confocal microscope with an incubation
334 chamber (LSM, 780) and the fiber optic was secured parfocally onto the objective turret using a custom fixture,
335 described in a previous work[41]. The microscope's 10x objective and programmable stage was used to visually locate
336 each sensor spot to ensure that the distance between the fiber optic and each sensor spot was consistent across all 96
337 devices. The fiber optic positions for all 96 devices were manually assigned and saved using the microscope's
338 software. A 2-point calibration of the oxygen sensors was performed using the FiresStingO$_2$ software. Microchannels
339 were filled with water and 30 g/L of sodium sulfite in water to obtain the high and low setpoint values corresponding
340 to 100% air saturated and 0% air saturated solutions, respectively. Measurement of steady state oxygen in a P96-O$_2$
341 plate was accomplished via automated and sequential positioning of the fiber optic beneath each device with a dwell
342 time of approximately 12 seconds per device as the FireStingO$_2$ acquired oxygen measurements at a sampling rate of
343 1 Hz. A custom-built algorithm in MATLAB was used to convert the raw data containing oxygen measurements
344 acquired at 1 Hz for an entire P96-O$_2$ plate into average readouts for each device in P96-O$_2$. Oxygen measurements
345 in each device were the average of 10-12 samples acquired at 1 Hz. Oxygen consumption was estimated as the
346 difference between steady state oxygen measurements in devices filled with air saturated culture medium and devices
347 containing culture medium and tissue.

Cisplatin treatment

349 cis-Diammineplatinum(II) dichloride (cisplatin) was purchased from Sigma, Aldrich (P4394-25MG) and dissolved
350 in 0.9% sodium chloride in water to form a 2380 μM stock solution. The stock solution was diluted in culture medium
351 to produce working concentrations of 0.5, 1, 3, 5, 10, 25, 100, and 200 μM. The vehicle group contained 8.4% sodium
352 chloride solution, which was equivalent to the concentration of sodium chloride solution used in the highest cisplatin
353 dose. Cisplatin doses were delivered via the inlets of the top and bottom microchannels of specified devices, shown
354 in the plate map in fig. S6. Oxygen was measured in the bottom microchannel of each device at 24 hr. timepoints for
355 the 9 doses of cisplatin ranging from 0-200 μM. Culture medium with the proper cisplatin dose was refreshed in each
356 device every 24 hours following oxygen measurements.

Lactate dehydrogenase (LDH) assay

358 The CyQUANT^{TM} LDH Cytotoxicity Assay (Thermo Fisher, USA), a standard colorimetric-based assay for assessing
359 cellular cytotoxicity, was used for quantifying extracellular lactate dehydrogenase (LDH) in the culture medium. 30
360 μL of culture medium was extracted from the inlet and outlet of each bottom microchannel following oxygen
361 measurements on day 7, 8, 9, 10, 11 (t= 24, 48, 72, 96, 120 hrs. following initial cisplatin exposure) and transferred
362 to a 96 well plate. Samples were subsequently transferred in duplicates to two 96 well plates. 15 μL of the
363 CyQUANT^{TM} LDH Cytotoxicity Assay reaction mixture was added to each medium sample for 30 minutes at room
364 temperature. Following 30 minutes, 15 μL of the CyQUANT^{TM} LDH Cytotoxicity Assay stop solution was added and
365 plates were centrifuged to remove any bubbles present in the wells. Absorbance was measured at 490 nm and 680 nm
366 in each well with a standard microplate reader. LDH content for each device was quantified from the absorbance
367 readings, as shown in equation 2 below, in which i represents the technical replicate number.

368
$$LDH = \sum_{i=1}^{2}(abs_{490} - abs_{680})_{cells} - (abs_{490} - abs_{680})_{medium\ only} \qquad (2)$$

369   Culture medium was refreshed following LDH measurements at 24 hr. timepoints. Cumulative LDH, the amount of
370   LDH released in the culture medium over multiple timepoints, was computed by summing LDH at each timepoint
371   with LDH from all previous timepoints.

372   **Immunofluorescent staining and imaging**

373   On day 11, hRPTECs and hMVECs were fixed with 4% paraformaldehyde (Thermo Fisher) in PBS for 10 minutes
374   followed by three rinses with PBS. Microchannels were filled with 0.1% Triton- X (Thermo Fisher, USA) with PBS
375   for 5 minutes to permeabilize the cells. Microchannels were blocked with 3% normal goat serum (NGS) in PBS for 1
376   hr. on a rocker at room temperature. Mouse primary ZO-1 antibodies (Abcam, USA) were diluted 1:200 in NGG and
377   incubated in each microchannel for 24 hrs. at 4° C. Microchannels were rinsed 3 times with PBS. Goat anti-mouse
378   secondary antibodies (IgG H&L Alexa Fluor 488, Thermo Fisher, USA) were diluted 1:250 in NGS. For labelling
379   nuclei and filamentous actin, Hoechst 33342 and Phalloidin-iFluor 633 were diluted 1:500 and 1:1000, respectively,
380   in NGS. Microchannels were filled with NGS containing secondary antibodies, nuclei, and filamentous actin labels
381   for 3 hrs. at room temperature on a rocker. Microchannels were rinsed 3 times with PBS prior to imaging. Images
382   were acquired with a scanning confocal microscope (Zeiss, LSM710) using a 40x water immersion objective and
383   lasers with excitations wavelengths of 405, 488, and 637 nm.

384   **hRPTEC nuclei count quantification**

385   Two 40x images of nuclei for 317 x 317 μm regions of interest were captured on the membrane on the left and right
386   side of the light absorbing sensor spot. Stardist[57], an open-source image processing pipeline in python, was used for
387   segmentation and counting of nuclei in each image. Nuclei counts were divided by the surface area of the region of
388   interest to compute nuclei density on the left and right side of the sensor. The nuclei densities on the left and right side
389   of the sensor were averaged to yield an averaged nuclei density for a single device.

390   **Mathematical modelling of dose response curves**

391   The dose response curves of cisplatin were computed using the standard Hill equation[58], shown in equation 3 below,
392   where x is the concentration, y_0 is the minimum response, y_∞ is the maximum response, H is the Hill coefficient
393   and x_{50} is the concentration resulting in 50% of a maximal response.

394
$$y_{hill} = y_0 + \frac{y_\infty - y_0}{1 + (\frac{x_{50}}{x})^H} \qquad (3)$$

395   Equation 3 was fitted to the experimental data via minimization of the least residual squares to compute predicted
396   dose response curves at each timepoint. The IC20, concentration resulting in 20% of maximal response, was computed
397   based on equation 4, where F is the percent response.

398
$$ICF = (\frac{F}{100 - F})^{1/H} * x_{50} \qquad (4)$$

399   All computational analysis related to fitting dose-response curves based on the Hill equation was performed using
400   custom-made pipelines in python with the SciPy module[59].

401   **Gaussian mixture model-based clustering**

402   Unsupervised clustering was performed based on probabilistic gaussian mixture models and implemented using the
403   Sklearn.mixture module in sci-kit learn[60]. Clusters were assumed to contain datapoints following a gaussian
404   distribution. The expectation-maximization algorithm[61] was implemented to return parameters for gaussian
405   distributions that resulted in the highest probability of containing the datapoints. For visualization purposes, the
406   optimized gaussian distributions were projected to two-dimensional space and represented as ellipses.

407   **Statistical analysis**

408 Data are presented as mean ± standard deviation of measurements. All *n* values represent the number of individual
409 devices per condition. Kruskal-Wallis & Dunn's post-hoc tests were used to calculate significant differences between
410 different groups. All statistical tests were performed in python using Scipy[59] and Sci-kit learn[60].

411 ## Author Contributions

Kann, Samuel H.	Designed/conceived measurement methodology, led and executed engineering and biological experiments, analyzed & interpreted data, wrote manuscript.
Shaughnessey, Erin M.	Executed biological experiments, supported development of measurement methodology, analyzed & interpreted data, wrote manuscript.
Zhang, Xin	Led experimental strategy, supported development of measurement methodology, analyzed & interpreted data, wrote manuscript, funding acquisition.
Charest, Joseph L.	Designed/conceived measurement methodology, designed/conceived platform technology, led experimental strategy, analyzed & interpreted data, wrote manuscript, funding acquisition.
Vedula, Else M.	Designed/conceived measurement methodology, Designed/conceived platform technology, led experimental strategy, analyzed & interpreted data, wrote manuscript, funding acquisition.

412

413 ## Conflicts of Interest

414 There are no conflicts to declare.

415 ## Acknowledgements

422 ## References

423 1 M. J. Wilmer, C. P. Ng, H. L. Lanz, P. Vulto, L. Suter-Dick and R. Masereeuw, *Trends in Biotechnology*,
424 2016, **34**, 156–170.

425 2 Kratz, Höll, Schuller, Ertl, and Rothbauer, *Biosensors*, 2019, **9**, 110.

426 3 Z. Pezeshki, A. Khosravi, M. Nekuei, S. Khoshnood, E. Zandi, M. Eslamian, A. Talebi, S. N. Emami and
427 M. Nematbakhsh, *J Nephropathol*, 2017, **6**, 163–167.

428 4 P. Zhang, J. Chen, Y. Wang, Y. Huang, Y. Tian, Z. Zhang and F. Xu, *Chem. Res. Toxicol.*, 2016, **29**, 776–
429 783.

430 5 H. Azizgolshani, J. R. Coppeta, E. M. Vedula, E. E. Marr, B. P. Cain, R. J. Luu, M. P. Lech, S. H. Kann, T.
431 J. Mulhern, V. Tandon, K. Tan, N. J. Haroutunian, P. Keegan, M. Rogers, A. L. Gard, K. B. Baldwin, J. C. de
432 Souza, B. C. Hoefler, S. S. Bale, L. B. Kratchman, A. Zorn, A. Patterson, E. S. Kim, T. A. Petrie, E. L. Wiellette, C.
433 Williams, B. C. Isenberg and J. L. Charest, *Lab Chip*, 2021, **21**, 1454–1474.

434 6 K. M. Bircsak, R. DeBiasio, M. Miedel, A. Alsebahi, R. Reddinger, A. Saleh, T. Shun, L. A. Vernetti and
435 A. Gough, *Toxicology*, 2021, **450**, 152667.

436 7 E. M. Vedula, J. L. Alonso, M. A. Arnaout and J. L. Charest, *PLOS ONE*, 2017, **12**, e0184330.

437 8 T. T. G. Nieskens, M. Persson, E. J. Kelly and A.-K. Sjögren, *Drug Metab Dispos*, 2020, **48**, 1303–1311.

438   9   K.-J. Jang, A. P. Mehr, G. A. Hamilton, L. A. McPartlin, S. Chung, K.-Y. Suh and D. E. Ingber, *Integrative*
439   *Biology*, 2013, **5**, 1119–1129.

440   10   S. K. Nigam, W. Wu, K. T. Bush, M. P. Hoenig, R. C. Blantz and V. Bhatnagar, *Clinical Journal of the*
441   *American Society of Nephrology*, 2015, **10**, 2039–2049.

442   11   Y. Duan, N. Gotoh, Q. Yan, Z. Du, A. M. Weinstein, T. Wang and S. Weinbaum, *Proceedings of the*
443   *National Academy of Sciences*, 2008, **105**, 11418–11423.

444   12   E. M. Frohlich, X. Zhang and J. L. Charest, *Integr. Biol.*, 2012, **4**, 75–83.

445   13   M. Essig, F. Terzi, M. Burtin and G. Friedlander, *American Journal of Physiology-Renal Physiology*, 2001,
446   **281**, F751–F762.

447   14   Q. Ren, M. L. Gliozzi, N. L. Rittenhouse, L. R. Edmunds, Y. Rbaibi, J. D. Locker, A. C. Poholek, M. J.
448   Jurczak, C. J. Baty and O. A. Weisz, *Traffic*, 2019, **20**, 448–459.

449   15   S. J. Kunnen, T. B. Malas, C. M. Semeins, A. D. Bakker and D. J. M. Peters, *Journal of Cellular*
450   *Physiology*, 2018, **233**, 3615–3628.

451   16   J. Vriend, J. G. P. Peters, T. T. G. Nieskens, R. Škovroňová, N. Blaimschein, M. Schmidts, R. Roepman, T.
452   J. J. Schirris, F. G. M. Russel, R. Masereeuw and M. J. Wilmer, *Biochimica et Biophysica Acta (BBA) - General*
453   *Subjects*, 2020, **1864**, 129433.

454   17   L. Yin, G. Du, B. Zhang, H. Zhang, R. Yin, W. Zhang and S.-M. Yang, *Sci Rep*, 2020, **10**, 6568.

455   18   G. Nowak and R. G. Schnellmann, *American Journal of Physiology-Cell Physiology*, 1995, **268**, C1053–
456   C1061.

457   19   P. Bhargava and R. G. Schnellmann, *Nat Rev Nephrol*, 2017, **13**, 629–646.

458   20   F. Tasnim and D. Zink, *American Journal of Physiology-Renal Physiology*, 2012, **302**, F1055–F1062.

459   21   S. Aydin, S. Signorelli, T. Lechleitner, M. Joannidis, C. Pleban, P. Perco, W. Pfaller and P. Jennings,
460   *American Journal of Physiology-Cell Physiology*, 2008, **294**, C543–C554.

461   22   E. M. Shaughnessey, S. H. Kann, H. Azizgolshani, L. D. Black, J. L. Charest and E. M. Vedula, *Sci Rep*,
462   2022, **12**, 13182.

463   23   M. T. Rogers, A. L. Gard, R. Gaibler, T. J. Mulhern, R. Strelnikov, H. Azizgolshani, B. P. Cain, B. C.
464   Isenberg, N. J. Haroutunian, N. E. Raustad, P. M. Keegan, M. P. Lech, L. Tomlinson, J. T. Borenstein, J. L. Charest
465   and C. Williams, *Sci Rep*, 2021, **11**, 12225.

466   24   A. L. Gard, R. J. Luu, C. R. Miller, R. Maloney, B. P. Cain, E. E. Marr, D. M. Burns, R. Gaibler, T. J.
467   Mulhern, C. A. Wong, J. Alladina, J. R. Coppeta, P. Liu, J. P. Wang, H. Azizgolshani, R. F. Fezzie, J. L. Balestrini,
468   B. C. Isenberg, B. D. Medoff, R. W. Finberg and J. T. Borenstein, *Sci Rep*, 2021, **11**, 14961.

469   25   A. Nicolas, F. Schavemaker, K. Kosim, D. Kurek, M. Haarmans, M. Bulst, K. Lee, S. Wegner, T.
470   Hankemeier, J. Joore, K. Domansky, H. L. Lanz, P. Vulto and S. J. Trietsch, *Lab Chip*, 2021, **21**, 1676–1685.

471   26   M. Azimzadeh, P. Khashayar, M. Amereh, N. Tasnim, M. Hoorfar and M. Akbari, *Biosensors (Basel)*,
472   2021, **12**, 6.

473   27   E. Tanumihardja, R. H. Slaats, A. D. van der Meer, R. Passier, W. Olthuis and A. van den Berg, *ACS Sens.*,
474   2021, **6**, 267–274.

475   28   A. Weltin, K. Slotwinski, J. Kieninger, I. Moser, G. Jobst, M. Wego, R. Ehret and G. A. Urban, *Lab Chip*,
476   2014, **14**, 138–146.

29   A. Moya, M. Ortega-Ribera, X. Guimerà, E. Sowade, M. Zea, X. Illa, E. Ramon, R. Villa, J. Gracia-Sancho and G. Gabriel, *Lab on a Chip*, 2018, **18**, 2023–2035.

30   O. S. Wolfbeis, *BioEssays*, 2015, **37**, 921–928.

31   S. M. Grist, L. Chrostowski and K. C. Cheung, *Sensors*, 2010, **10**, 9286–9316.

32   J. Ehgartner, P. Sulzer, T. Burger, A. Kasjanow, D. Bouwes, U. Krühne, I. Klimant and T. Mayr, *Sensors and Actuators B: Chemical*, 2016, **228**, 748–757.

33   M. Koopman, H. Michels, B. M. Dancy, R. Kamble, L. Mouchiroud, J. Auwerx, E. A. A. Nollen and R. H. Houtkooper, *Nat Protoc*, 2016, **11**, 1798–1816.

34   P. Wolf, M. Brischwein, R. Kleinhans, F. Demmel, T. Schwarzenberger, C. Pfister and B. Wolf, *Biosensors and Bioelectronics*, 2013, **50**, 111–117.

35   M. Busche, D. Rabl, J. Fischer, C. Schmees, T. Mayr, R. Gebhardt and M. Stelzle, *EXCLI Journal; 21:Doc144; ISSN 1611-2156*, , DOI:10.17179/EXCLI2021-4351.

36   H. Zirath, S. Spitz, D. Roth, T. Schellhorn, M. Rothbauer, B. Müller, M. Walch, J. Kaur, A. Wörle, Y. Kohl, T. Mayr and P. Ertl, *Lab Chip*, 2021, 10.1039.D1LC00528F.

37   R. Krenger, M. Cornaglia, T. Lehnert and M. A. M. Gijs, *Lab Chip*, 2020, **20**, 126–135.

38   F. Bunge, S. van den Driesche, M. Waespy, A. Radtke, G. Belge, S. Kelm, A. M. Waite, U. Mirastschijski and M. J. Vellekoop, *Sensors and Actuators B: Chemical*, 2019, **289**, 24–31.

39   S. A. Mousavi Shaegh, F. De Ferrari, Y. S. Zhang, M. Nabavinia, N. Binth Mohammad, J. Ryan, A. Pourmand, E. Laukaitis, R. Banan Sadeghian, A. Nadhman, S. R. Shin, A. S. Nezhad, A. Khademhosseini and M. R. Dokmeci, *Biomicrofluidics*, 2016, **10**, 044111.

40   B. Müller, P. Sulzer, M. Walch, H. Zirath, T. Buryška, M. Rothbauer, P. Ertl and T. Mayr, *Sensors and Actuators B: Chemical*, 2021, **334**, 129664.

41   S. H. Kann, E. M. Shaughnessey, J. R. Coppeta, H. Azizgolshani, B. C. Isenberg, E. M. Vedula, X. Zhang and J. L. Charest, *Microsyst Nanoeng*, 2022, **8**, 109.

42   E. H. J. Verschuren, C. Castenmiller, D. J. M. Peters, F. J. Arjona, R. J. M. Bindels and J. G. J. Hoenderop, *Nat Rev Nephrol*, 2020, **16**, 337–351.

43   A. Weltin, S. Hammer, F. Noor, Y. Kaminski, J. Kieninger and G. A. Urban, *Biosensors and Bioelectronics*, 2017, **87**, 941–948.

44   A. A. Gerencser, A. Neilson, S. W. Choi, U. Edman, N. Yadava, R. J. Oh, D. A. Ferrick, D. G. Nicholls and M. D. Brand, *Anal. Chem.*, 2009, **81**, 6868–6878.

45   H. J. Kim and D. E. Ingber, *Integr. Biol.*, 2013, **5**, 1130.

46   T.-E. Park, N. Mustafaoglu, A. Herland, R. Hasselkus, R. Mannix, E. A. FitzGerald, R. Prantil-Baun, A. Watters, O. Henry, M. Benz, H. Sanchez, H. J. McCrea, L. C. Goumnerova, H. W. Song, S. P. Palecek, E. Shusta and D. E. Ingber, *Nat Commun*, 2019, **10**, 2621.

47   K. Tan, P. Keegan, M. Rogers, M. Lu, J. R. Gosset, J. Charest and S. S. Bale, *Lab Chip*, 2019, **19**, 1556–1566.

48   P. Salem, M. Khalyl, K. Jabboury and L. Hashimi, *Cancer*, 1984, **53**, 837–840.

49   C. Tang, M. J. Livingston, R. Safirstein and Z. Dong, *Nat Rev Nephrol*, 2022, 1–20.

515   50   A. Hill, *Journal of Physiology*, 1910, 40iv-vii.

516   51   S. Goutelle, M. Maurin, F. Rougier, X. Barbaut, L. Bourguignon, M. Ducher and P. Maire, *Fundamental &*
517   *Clinical Pharmacology*, 2008, **22**, 633–648.

518   52   A. Cohen, K. Ioannidis, A. Ehrlich, S. Regenbaum, M. Cohen, M. Ayyash, S. S. Tikva and Y. Nahmias,
519   *Sci. Transl. Med.*, 2021, **13**, eabd6299.

520   53   M. W. van der Helm, O. Y. F. Henry, A. Bein, T. Hamkins-Indik, M. J. Cronce, W. D. Leineweber, M.
521   Odijk, A. D. van der Meer, J. C. T. Eijkel, D. E. Ingber, A. van den Berg and L. I. Segerink, *Lab Chip*, 2019, **19**,
522   452–463.

523   54   M. K. Vormann, L. Gijzen, S. Hutter, L. Boot, A. Nicolas, A. van den Heuvel, J. Vriend, C. P. Ng, T. T. G.
524   Nieskens, V. van Duinen, B. de Wagenaar, R. Masereeuw, L. Suter-Dick, S. J. Trietsch, M. Wilmer, J. Joore, P.
525   Vulto and H. L. Lanz, *The AAPS Journal*, 2018, **20**, 90.

526   55   A. Agarwal, J. A. Goss, A. Cho, M. L. McCain and K. K. Parker, *Lab Chip*, 2013, **13**, 3599.

527   56   G. J. McLachlan and K. E. Basford, *Mixture models. Inference and applications to clustering*, 1988.

528   57   U. Schmidt, M. Weigert, C. Broaddus and G. Myers, in *Medical Image Computing and Computer Assisted*
529   *Intervention – MICCAI 2018*, eds. A. F. Frangi, J. A. Schnabel, C. Davatzikos, C. Alberola-López and G. Fichtinger,
530   Springer International Publishing, Cham, 2018, pp. 265–273.

531   58   R. L. Prentice, *Biometrics*, 1976, **32**, 761–768.

532   59   SciPy 1.0: fundamental algorithms for scientific computing in Python | Nature Methods,
533   https://www.nature.com/articles/s41592-019-0686-2?report=reader, (accessed November 1, 2022).

534   60   F. Pedregosa, G. Varoquaux, A. Gramfort, V. Michel, B. Thirion, O. Grisel, M. Blondel, P. Prettenhofer, R.
535   Weiss, V. Dubourg, J. Vanderplas, A. Passos, D. Cournapeau, M. Brucher, M. Perrot and É. Duchesnay, *Journal of*
536   *Machine Learning Research*, 2011, **12**, 2825–2830.

537   61   A. P. Dempster, N. M. Laird and D. B. Rubin, *Journal of the Royal Statistical Society: Series B*
538   *(Methodological)*, 1977, **39**, 1–22.

539